Control Performance Characterization and Monitoring Scheme for Power Converters in Weak Grids

JIACHEN WANG (Student Member, IEEE), QING LIU (Member, IEEE), XIANGCHEN ZENG, WEIJIAN HAN (Member, IEEE), AND ZHEN XIN (Member, IEEE)

State Key Laboratory of Reliability and Intelligence of Electrical Equipment, Hebei University of Technology, Tianjin 300130, China

CORRESPONDING AUTHOR: QING LIU (e-mail: qing.liu@hebut.edu.cn)

ABSTRACT In weak grids, control performance of power converters is negatively affected by the significantly varied grid impedance, which can easily lead to degradation of anti-harmonic performance, resonances or even system instability. A rapid control performance monitor is therefore proposed in this work to acquire power converters' actual performance indexes, i.e., the crossover frequency and phase margin. With the measured real-time information, important functions like health management, control parameters design and adaptive control of power systems can be conveniently realized. The monitor is implemented by perturbating the control loop of the power converter under test with a frequency-autotuned small signal, showing satisfying dynamic response and anti-noise performance. Thanks to the 100% digital implementation, the proposed performance monitor requires no extra hardware and no further cost. The detailed design of the monitor, based on small signal models derivation employing an envelope modeling method, is presented in this article. Extensive experiments were carried out to verify the efficacy of the proposed monitor.

INDEX TERMS Digital control, loop gain, stability margin, weak grids.

I. INTRODUCTION

Power systems are experiencing an evolution from the stiff grid to the weak grid accompanied with the widespread integration of renewables through power converters [1], [2], [3]. Thanks to the intermittent gene of renewables and the nonlinearity of power converters, weak grids rich in green renewables are indeed unfriendly to the existing power grids and customers, which may lead to severe stability problems. Those converter modules may connect in series as usually done in medium-voltage multi-stage systems, or they may be connected in parallel at point of common coupling (PCC). Due to the varying power absorption from loads and the intermittent power generation from renewables, parameters of converters highly permeated grids vary significantly both from point to point and over time, showing typical weak grid behaviors [4].

In power systems, converters' key state variables (e.g., inductor current and capacitor voltage) are usually closed-loop controlled to achieve: i) system stability, i.e., system tracks the reference asymptotically; and ii) disturbance rejection to guarantee robust operation [5], [6]. For these purposes, it is essential to design a control loop with guaranteed stability and high dynamic performance. Controllers of power converters are theoretically designed based on the open-loop transfer function derived from the small signal model, referring to specific requirements, such as bandwidth (BW) and phase margin (PM). However, it is almost impossible to achieve the required control performance precisely in practice, due to the inherent system aging and manufacturing tolerance. In addition to the long-term scale variations, more significant deviations are found in weak grids where large and prompt impedance changes are commonly confronted. For example, controller's BW and PM of grid-tied inverters can be changed by 50% due to grid impedance variations in weak grids, which results in severe negative impacts on control performance

of power converters in terms of both dynamics and stability [7].

For this issue, three types of solutions can be identified: i) *Conservative controller design* [8], by intentionally reducing the design requirements with narrower BW and larger PM to embrace greater system parameter variations; ii) *Impedance reshaping* [9], [10], by modifying the output impedance of converters based on minor loop gain defined as the ratio between the converter output impedance and the grid impedance; and iii) *Loop gain based adaptive control* [11], [12], by adjusting control parameters adaptively according to the real-time measured information of controller's actual loop gain. Compared to the previous methods, the third loop gain based solution finds greater interest because it focuses directly on the control performance and requires no information about the grid impedance.

Different measurement methods of the loop gains and stability margins under various conditions are reported in literature. Prof. Middlebrook kicked-off the research of loop gain measurement by proposing an off-line small signal injection technology in [13]. Based on it, a series of loop gain measurement approaches were introduced, which can be generally categorized into: sine-sweep monitors [14], [15] and wide-band monitors [16], [17]. Sine-sweep monitors usually take few seconds to complete a precise loop gain measurement [14], [15]. To curtail the measurement time, different wide-band small signals (e.g., Pseudo-Random Binary Sequence, PRBS [17]) were adopted to accelerate the loop gain measurement with only one injection [16]. Hence, the measurement time is successfully reduced to hundreds of milliseconds (measured spectra: 100 Hz–100 kHz). In practical, to ensure the measurement accuracy, multiple injections are actually required. The long measurement time prohibited its wide implementation in adaptive control. To further reduce the measurement time, researchers only sketch the BW and PM of a control loop by perturbating mainly around the crossover frequency [18], [19]. So doing, tens of milliseconds level loop gain measurement was achieved. However, these methods, such as peak sampling method [18], mainly performed in DC microgrids with minor background harmonics. Even if the coordinate projection method is applied to AC microgrids [12], it employs many redundant filters to ensure accuracy, resulting in long measurement time and unsatisfying dynamics.

To address these issues, a control performance monitor for power converters in weak grids is proposed in this work. The proposed monitor shows very short measurement time (few ms) and reduced computational burden. Additionally, multiple advantages can be identified: The monitor i) can operate without breaking the feedback loops; and ii) is highly robust to background harmonics while guaranteeing iii) relatively low invasiveness to power grids. The method facilitates implementation of high performance control, like optimization control of parallelly operated converters, maximum allowable bandwidth tracking control, etc. [19], [20] and allows other applications such as control parameters design, health supervision, adaptive control, etc. [11], [12], [21], [22].
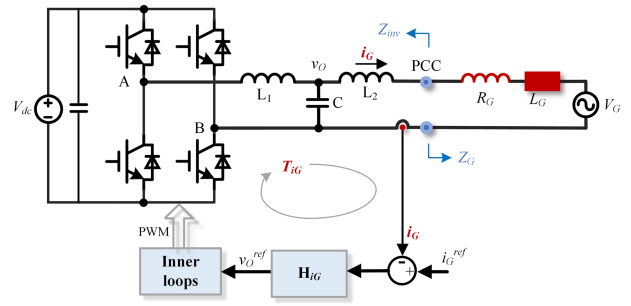

FIGURE 1. Single-phase grid-tied inverter system.

The rest of work is arranged as follows. Section II is a brief introduction of the considered scenario. Next, Section III introduces the proposed monitor and its small signal model. While, design method is covered in Section IV. Experimental verification and conclusions are given in Sections VI and VII, respectively.

II. SCENARIO OF INTEREST
Without loss of generality, as shown in Fig. 1, we take a classical single-phase grid-tied power system as an example. For simplicity, the multiple power conversion stages are collapsed in an ideal DC source v_{DC} and the grid impedance Z_G is modelled as an inductor L_G in series with a resistance R_G [23]. To pursuit high power quality on AC side, as depicted in Fig. 1, grid current i_G is usually feedback and controlled as the external loop in grid-tied inverters [24]. Seen from PCC, the inductor L_2 is coupled with external power grid v_G through the grid impedance Z_G, so control performance of i_G loop is directly affected by grid-inverter interactions, which can result in poor power quality or even instability in weak grids.

To characterize the control performance of converters operating in weak grids, commonly used analysis methods are mainly based either on the information of inverter-grid impedance ratio [23] or the loop gain [25]. The impedance ratio characterization method, however, is not fast enough for critical applications with high dynamics like weak grids. Additionally, it is highly intrusive and requires extra hardware since it usually needs to break the power circuit so that a signal generator can be implemented to measure the impedances. For these reasons, the loop gain-based control performance characterization approach is gaining weight over time, which will be analyzed in detail as follows.

The small signal model of the considered single-phase grid-tied power system is shown in Fig. 2 [26]. Where, $W_{vo}(s)$ can be obtained by transforming $W_{v_O}(z)$ into the S-domain. And $W_{v_O}(z)$ is the closed loop transfer function of the inner control loops, which can be expressed as

$$W_{v_O}(z) = \frac{v_O(z)}{v_O^{ref}(z)} = 1/(z^2 - 2z + 1). \quad (1)$$

$H_{iG}(s) = K_p + K_i \cdot \frac{1}{s}$ is the compensator of the grid current loop; $Z_{L2}(s) = sL_2$ is the impedance of the grid-side inductance; $Z_G(s) = R_G + sL_G$ is the grid impedance; $Z_{O,v_O}(s)$ is
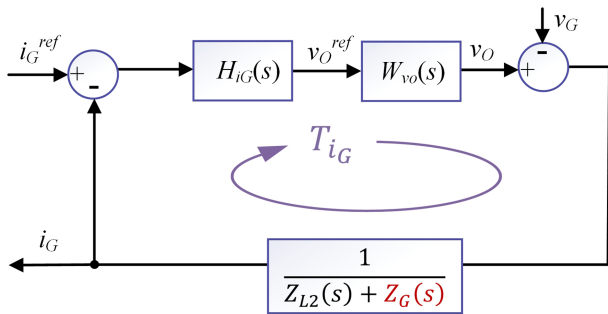
FIGURE 2. Small signal model of the single phase grid-connected system.
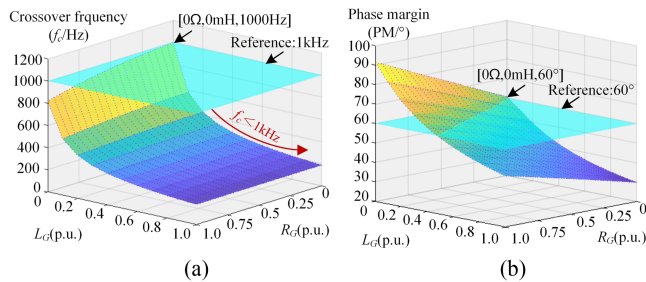

(a)   (b)

FIGURE 3. Relationships between control performance indexes and grid impedance. (a) Crossover frequency affected by Z_G; (b) phase margin affected by Z_G.

the output impedance of inverter. Hence, the open-loop transfer function $T_{iG}(s)$ can then be derived as

$$T_{iG}(s) = \frac{W_{vo}(s) \cdot H_{iG}(s)}{Z_{O,v_O}(s) + Z_{L2}(s) + Z_G(s)}. \tag{2}$$

As can be seen, $T_{iG}(s)$ integrates the information of both the inverter and the grid impedance. Any changes in the inverter or the grid impedance will be directly reflected into the variations of the open-loop gain. The issue is more serious in weak grids with large and variant grid impedance Z_G. On this basis, the control performance can be quantitatively characterized by the open-loop gain with control indexes like crossover frequency f_c (approximate to the BW practically) and PM.

Fig. 3 graphically illustrates the relationship between control performance indexes and the grid impedance. The overall trend is that the crossover frequency decreases as the grid impedance increases; the PM decreases with the increase of the inductive portion and the decrease of the resistive portion. Hence, to guarantee stability and high performance control, the actual loop gain should be online measured.

III. MECHANISM AND MODELLING OF THE CONTROL PERFORMANCE MONITOR

As depicted in Fig. 4, a rapid control performance monitor with satisfying dynamic response and superior harmonic rejection capability is proposed in this work to acquire grid-tied inverters' control performance indexes crossover frequency and PM continuously. The proposed performance monitor is structurally composed of four parts: i) a signal generator, ii) a pair of signal extractors, iii) a pair of amplitude-phase
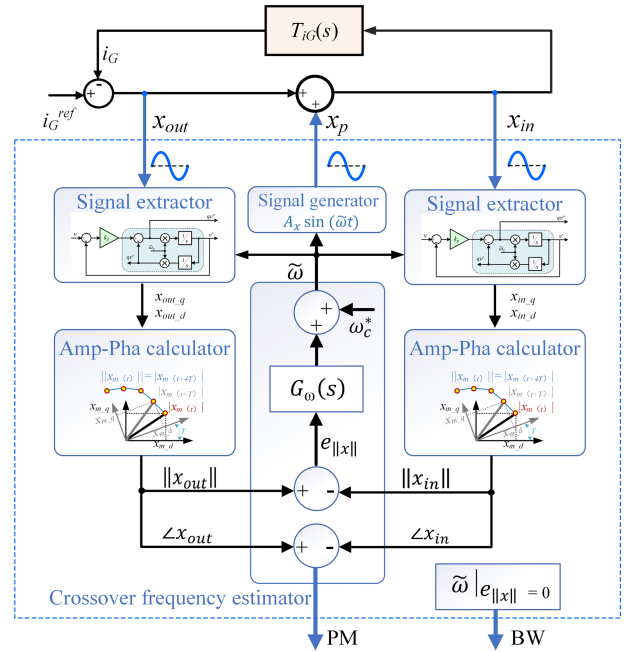

FIGURE 4. Structure of the proposed control performance monitor.
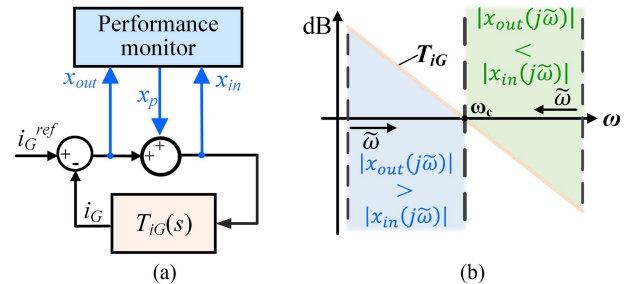

(a)   (b)

FIGURE 5. Middlebrook's loop gain monitoring technology. (a) System structure; (b) estimation principle of the crossover frequency.

calculators and iv) a crossover frequency estimator. Detailed principles of the proposed online performance monitor are now introduced as follows.

A. MIDDLEBROOK'S LOOP GAIN MONITORING TECHNOLOGY

In this subsection, we present the necessary theoretical and mathematical background of Middlebrook's loop gain measurement strategy ([13], [27]) that will be harnessed in the later sections.

As shown in Fig. 5(a), $T_{iG}(s)$ (see (3)) is the open-loop transfer function of the considered single phase grid-tied power system. A sinusoidal perturbating signal $x_p(s)$ (digitally generated by the converter controller) is injected into the control loop under normal operation. The response signals ($x_{in}(s)$ and $x_{out}(s)$) before and after the injecting point can be expressed as:

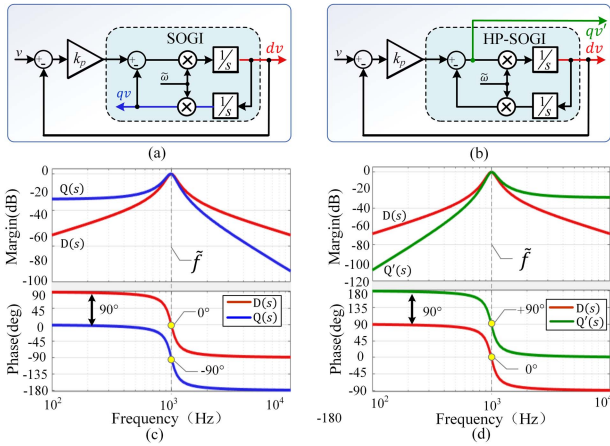$$x_{in}(s) = \frac{1}{1 + T_{iG}(s)} x_p(s) \tag{3}$$

FIGURE 6. The proposed signal extractor. (a) Structure of SOGI; (b) structure of HP-SOGI; (c) bode diagram of $D(s)$ and $Q(s)$; (d) bode diagram of $D(s)$ and $Q'(s)$.

$$x_{out}(s) = -\frac{T_{iG}(s)}{1 + T_{iG}(s)} x_p(s). \tag{4}$$

Then, $T_{iG}(s)$ can be represented as:

$$T_{iG}(s) = -\frac{x_{out}(s)}{x_{in}(s)}. \tag{5}$$

According to Fig. 5(b), the open-loop transfer function is monotonic around the crossover frequency ω_c, and only at ω_c, the loop gain satisfies

$$|T_{iG}(j\tilde{\omega})| = \frac{|x_{out}(j\tilde{\omega})|}{|x_{in}(j\tilde{\omega})|} = \frac{|x_{out}(j\omega_c)|}{|x_{in}(j\omega_c)|} = 1. \tag{6}$$

Accordingly, the PM can be calculated by

$$PM = \pi + \angle T_{iG}(j\omega_c) = \pi + \angle T_{iG}(j\tilde{\omega}). \tag{7}$$

B. SIGNAL GENERATOR

As shown in Fig. 4, the signal generator is designed to produce a small sinusoidal signal $x_p(j\tilde{\omega})$ with fixed amplitude and changeable frequency, which is injected into the control loop under test. Different from traditional analog impedance monitors, the proposed control performance monitor is 100% digitally implemented in the controller of power converters. Concretely, the perturbating signal $x_p(j\tilde{\omega})$ is implemented by a sinusoidal function whose amplitude A_x is fixed (designed in Section IV-B) and the frequency is updated by the output signal $\tilde{\omega}$ of the crossover frequency estimator (see Section III-E).

C. SIGNAL EXTRACTOR

Due to the presence of background harmonics in the monitoring signals (x_{in} and x_{out}), the signal extractor is designed to extract signals at perturbating frequency by filtering out the fundamental signal i_G and all the background harmonics.

Naturally, a band-pass filter is recommended thanks to its high harmonic rejection performance. As depicted in Fig. 6(a), it can be implemented by an adaptive second order generalized integrator (SOGI) structure, where the resonant

frequency of the SOGI is synchronized with the perturbation frequency $\tilde{\omega}$. Outputs (dv and qv) of the adaptive SOGI are exactly a pair of quadrature signals with respect to the input signal v, corresponding transfer functions are plotted in Fig. 6(c) and expressed as:

$$D(s) = \frac{dv(s)}{v(s)} = \frac{k_p \tilde{\omega} s}{s^2 + k_p \tilde{\omega} s + \tilde{\omega}^2} \tag{8}$$

$$Q(s) = \frac{qv(s)}{v(s)} = \frac{k_p \tilde{\omega}^2}{s^2 + k_p \tilde{\omega} s + \tilde{\omega}^2}. \tag{9}$$

However, according to IEEE standard 1547-2018 [28], harmonics of AC microgrids are mainly below 1.05 kHz (the 21st harmonic) at odd multiples of the fundamental frequency. The main harmonic spectra are below the crossover frequency of power converters, which is usually designed above 1 kHz for better dynamics. However, $Q(s)$ is a low-pass filter with cutoff frequency $\tilde{\omega} = 2\pi \tilde{f}$, which is unable to filter out the fundamental signal and multiple low frequency harmonics in AC grids. To solve this issue, a high-pass filter $Q'(s)$ is more preferable than the low-pass filter $Q(s)$, the corresponding transfer function is plotted in Fig. 6(d) and can be expressed as

$$Q'(s) = \frac{qv'(s)}{v(s)} = \frac{k_q s^2}{s^2 + k_q \tilde{\omega} s + \tilde{\omega}^2}. \tag{10}$$

Herein, $qv'(s)$ is designed to be quadrature to $v(s)$ and with $180°$ shifted in phase with respect to $qv(s)$.

Combining (8), (9) and (10), we can prove that the equation:

$$Q'(s) = [1 - D(s)] * k_p - Q(s) \tag{11}$$

holds correct only when $k_q = k_p$. That means $qv'(s)$ can be achieved by:

$$qv'(s) = (v(s) - dv(s)) * k_p - qv(s), \tag{12}$$

as implemented in Fig. 6(b). To differentiate with the original SOGI, the proposed high-pass filter is denoted as HP-SOGI. A similar implementation can be found in [29] for the purpose of active damping of LCL filters.

By this artificial design, three advantages can be achieved simultaneously: i) the classical SOGI structure is preserved so that the parameter design is convenient and standardized, while ii) the harmonics rejection performance of the monitor is significantly improved, and thus iii) no more redundant filters are needed for the next step amplitude and phase calculator.

D. AMPLITUDE-PHASE CALCULATOR

Assuming a perturbation signal $x_p(t) = B_x \sin(\tilde{\omega} t)$ is injected into the loop under test, the generated monitoring signals $x_{in}(t)$ and $x_{out}(t)$ can be defined uniformly as $x_m(t) = B_x \sin(\tilde{\omega} t)$, the resulting quadrature signals are then derived as [30]

$$dv(t) = -\frac{B_x}{\sqrt{1 - \frac{k_p^2}{4}}} \sin\left(\tilde{\omega}\sqrt{1 - \frac{k_p^2}{4}} t\right) e^{-\frac{k_p \tilde{\omega} t}{2}}$$
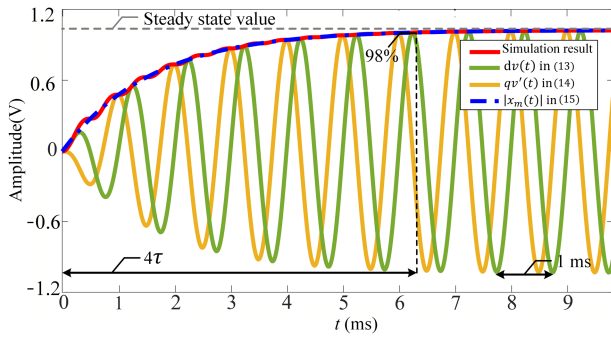
FIGURE 7. Theoretical step response and simulation results of the proposed amplitude-phase calculator.

FIGURE 8. Bode plots of $D(s)$ and $Q'(s)$ under variations of k_p. (a) Bode plots of $D(s)$; (b) bode plots of $Q'(s)$.

$$+ B_x \sin(\tilde{\omega} t) \approx B_x \left(1 - e^{-\frac{k_p \tilde{\omega} t}{2}}\right) \sin(\tilde{\omega} t) \quad (13)$$

$$qv'(t) = -\frac{B_x}{\sqrt{1 - \frac{k_p^2}{4}}} \cos\left(\tilde{\omega}\sqrt{1 - \frac{k_p^2}{4}} t - \varphi\right) e^{-\frac{k_p \tilde{\omega} t}{2}}$$

$$+ B_x \cos(\tilde{\omega} t) \approx B_x \left(1 - e^{-\frac{k_p \tilde{\omega} t}{2}}\right) \cos(\tilde{\omega} t) \quad (14)$$

on condition that $\tilde{\omega} >> k_p \tilde{\omega}/2$, $\varphi = arctan\frac{k_p/2}{\sqrt{1 - k_p^2/4}} \approx 0$.

Accordingly, the envelope of the monitoring signal $|x_m(t)|$ can be calculated by

$$|x_m(t)| = \sqrt{dv(t)^2 + qv'(t)^2}$$

$$= B_x \left(1 - e^{-\frac{k_p \tilde{\omega} t}{2}}\right), \quad (15)$$

which is equivalent to a first-order system with a time constant of $\tau = 2/(k_p \tilde{\omega})$. As verified in Fig. 7, the step response of $|x_m(t)|$ can convergent to 98% of the steady-state value in just 4τ, which is consistent with the theoretical response of a typical first order system.

Therefore, amplitude of the monitoring signal $\|x_m(t)\|$ is achieved from the steady-state value of $|x_m(t)|$ through

$$\|x_m(t)\| = |x_m(t)||_{t \geq 4\tau}. \quad (16)$$

Concurrently, the phase of the input signal $\angle x_m(t)$ can be calculated conveniently by

$$\angle x_m(t) = \arctan \frac{dv(t)}{qv'(t)}. \quad (17)$$

E. CROSSOVER FREQUENCY ESTIMATOR
Based on (6), the crossover frequency of the loop under test is estimated by means of a compensator

$$\tilde{\omega} = \omega_c^* + G_\omega (|x_{out}(t)| - |x_{in}(t)|). \quad (18)$$

where, ω_c^* is the theoretical crossover frequency, G_ω is the compensator.

As can be seen from (18) and observed from Fig. 4, the perturbation frequency $\tilde{\omega}$ is autonomously adjusted by
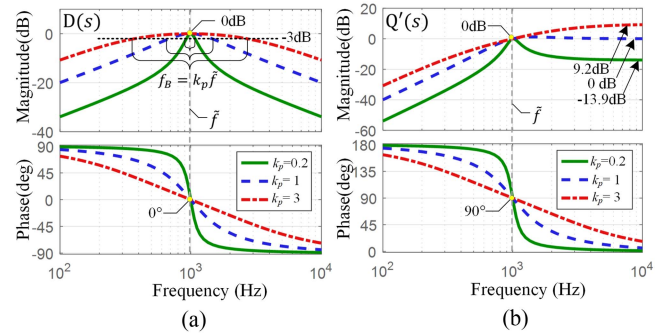
the amplitude difference of the monitoring signals. When $\|x_{out}(t)\| = \|x_{in}(t)\|$, the crossover frequency of the loop under test, approximately equals to the control bandwidth (BW), is estimated as

$$BW \approx \omega_c = \tilde{\omega}|_{e_{|x|=0}}. \quad (19)$$

And according to (7) and (17), the PM can be estimated by

$$PM = (\angle x_{out} - \angle x_{in})|_{e_{|x|=0}}. \quad (20)$$

IV. PARAMETERS DESIGN AND ANALYSIS
A. DESIGN OF THE SIGNAL EXTRACTOR
As shown in Fig. 6, the signal extractor is implemented by means of a HP-SOGI, whose performance is determined by the gain k_p. To design this gain properly, following conditions should be satisfied concurrently:

i) $\tilde{\omega} >> k_p \tilde{\omega}/2$;

ii) $\varphi = arctan\frac{\frac{k_p}{2}}{\sqrt{1 - k_p^2/4}} \approx 0$;

iii) low gain above the cut-off frequency $\tilde{\omega}$ of the high-pass filter $Q'(s)$ for overall satisfying harmonic attenuation (see Fig. 8(b));

iv) high quality factor Q_B of the band-pass filter $D(s)$ (see Fig. 8(a)) for outstanding signal extraction.

$$Q_B = \frac{\tilde{\omega}}{\omega_B} = \frac{1}{k_p}. \quad (21)$$

Herein, condition i) and ii) are based on the assumptions of (13) and (14), ω_B is the filter's bandwidth corresponding to -3 dB gain reduction.

As a rule of thumb, it is reasonable to consider "much bigger than" in the first condition i) equivalent to "an order of magnitude bigger than", so that $0 < k_p \leq 0.2$ holds. While the function of $\varphi(k_p)$ is plotted in Fig. 9, based on which, the condition ii) is replaced by $\varphi \leq 0.1$. Additionally, $|Q'(s)| \leq 0.707$ at high frequency and $5 \leq Q_B \leq 10$ are considered respectively for condition iii) and condition iv). According to the above analysis, the gain k_p should be designed as $0.1 \leq k_p \leq 0.2$, so that $k_p = 0.2$ is selected in this work.
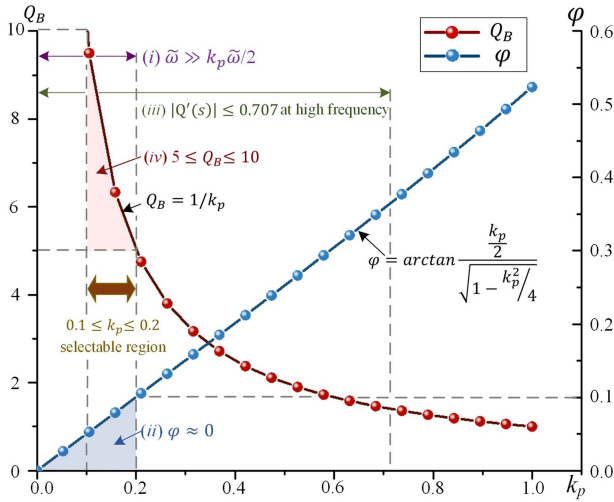
FIGURE 9. Parameters design of the signal extractor.

B. AMPLITUDE DESIGN OF THE INJECTED SIGNAL

Every coin has two sides. The perturbating signal is, on the one hand, necessary for monitoring of the control performance, as is widely done in impedance analyzers. On the other hand, it is a source of pollution that decreases the power quality. To guarantee reliable monitoring results and prevent unnecessary distortions, amplitude of the injected small signal should be carefully designed.

In principle, the minimum amplitude value of the injected signal equals to the ± 1 least significant bit of the ADC applied [18]. However, to extract the injected perturbation signals $x_{out}(j\tilde{\omega})$ and $x_{in}(j\tilde{\omega})$ from the fundamental signal and background harmonics, magnitude of the output signal after the HP-SOGI at perturbating frequency should be at least 3 dB higher than other frequencies. Taking x_{out} as an example, according to Fig. 4,

$$x_{out} = i_G^{ref}(j\omega_0) - i_G(j\omega_0) - \sum_{i=3}^{n} x_{out}(j\omega_i)$$

$$- \frac{T_{iG}(j\tilde{\omega})}{1 + T_{iG}(j\tilde{\omega})} x_p(j\tilde{\omega}) \qquad (22)$$

where, the maximum value of the fundamental component $\left(x_{out}(j\omega_0) = i_G^{ref}(j\omega_0) - i_G(j\omega_0)\right)$ equals to the nominal grid current I_{GN}, which is much higher than the harmonics $(i_G(j\omega_i), i = 3, 5, 7 \ldots)$.

After the proposed HP-SOGI, we achieve

$$Dx_{out} = Dx_{out}(j\omega_0) - \sum_{i=3}^{n} Dx_{out}(j\omega_i) - \ldots - Dx_{out}(j\tilde{\omega})$$

$$\qquad (23)$$

$$Q'x_{out} = Q'x_{out}(j\omega_0) - \sum_{i=3}^{n} Q'x_{out}(j\omega_i) - \ldots - Q'x_{out}(j\tilde{\omega})$$

$$\qquad (24)$$

Assuming that $Dx_{out}(j\omega_0) = D(j\omega_0) \cdot I_{GN}$, $Dx_{out}(j\omega_i) = D(j\omega_i) \cdot 0.05 I_{GN}$ and the value of $Dx_{out}(j\tilde{\omega})$ can be approximated as $\frac{1\angle -PM^*}{1 + 1\angle -PM^*} \cdot |x_p|$, the same goes for $Q'x_{out}$. Then the minimum amplitude of the injected signal can be calculated by

$$\begin{cases} |Dx_{out}(j\omega_i)| < |Dx_{out}(j\tilde{\omega})| - 3dB \\ |Q'x_{out}(j\omega_i)| < |Q'x_{out}(j\tilde{\omega})| - 3dB \end{cases}, \ i = 0, 3, 5, \ldots$$

$$\qquad (25)$$

Similar analysis can be applied to x_{in} as well.

Based on which, the amplitude of $|x_p|$ is designed as 2.5% of the grid nominal current in this work.

C. DESIGN OF THE COMPENSATOR G_ω

To design the parameters of the compensator G_ω, the open-loop transfer function $e_{|x_m|}(s)/\tilde{\omega}(s)$ needs to be derived first. Here, assuming that a step change is applied to $\|x_m(s)\|$, the transfer function between $\|x_m(s)\|$ and $|x_m(s)|$ can be derived as

$$\frac{|x_m(s)|}{\|x_m(s)\|} = \frac{1}{\frac{2}{k_p\tilde{\omega}}s + 1}. \qquad (26)$$

The amplitude error $e_{\|x_m\|}(s)$ can then be presented as a function of $|x_p(s)|$ according to (4) and (5),

$$e_{|x|}(s) = [|x_{out}(s)| - |x_{in}(s)|]$$

$$= [\|x_{out}(s)\| - \|x_{in}(s)\|] \cdot \frac{|x_m(s)|}{\|x_m(s)\|}$$

$$= \frac{|T_{iG}(s)| - 1}{|1 + T_{iG}(s)|} \cdot |x_p(s)| \cdot \frac{|x_m(s)|}{\|x_m(s)\|}. \qquad (27)$$

Assuming the relationship between small signal variations of $\tilde{\omega}$ and $\|x_m(s)\|$ is simultaneous with respect to the amplitude estimation part $\frac{|x_m(s)|}{\|x_m(s)\|}$, thus gain of the former part can be approximated by the partial derivative of the steady-state value of (27) at $\tilde{\omega}$,

$$e_{|x|}(j\tilde{\omega})|_{dc} = \frac{|T_{iG}(j\tilde{\omega})| - 1}{|1 + T_{iG}(j\tilde{\omega})|} \cdot |x_p(j\tilde{\omega})|. \qquad (28)$$

Finally, with the hypothesis above, the loop gain to be compensated by the regulator G_ω is given by:

$$\frac{e_{|x|}(s)}{\tilde{\omega}(s)} = \frac{\partial e_{|x|}(s)|_{dc}}{\partial \tilde{\omega}(s)} \cdot \frac{1}{\frac{2}{k_p\tilde{\omega}}s + 1}. \qquad (29)$$

The regulator G_ω can then be designed following any standard procedure based on (29).

V. EXPERIMENTAL VERIFICATION

The experimental prototype considered in this article (structured as Fig. 1) is a 3 kVA single-phase grid-tied inverter system controlled by a triple-loop nested controller [26], as shown in Fig. 10. The controller is implemented in an NI cRIO-9057 platform and main system parameters are outlined in Table 1. The crossover frequency and PM of the external grid current loop in ideal girds (i.e., $Z_G = 0$) are designed as 1 kHz and 60°, respectively.
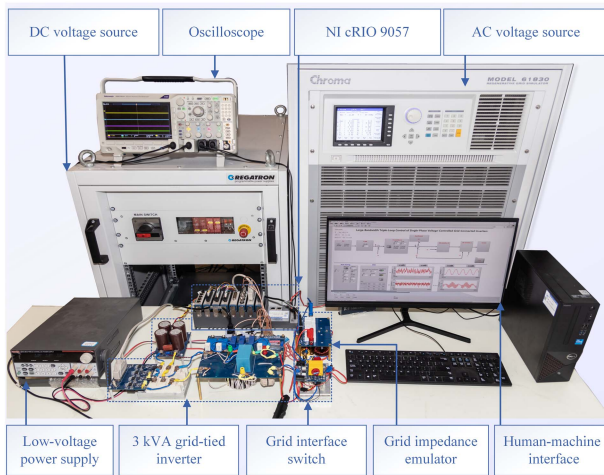
FIGURE 10. Testbench of 3 kVA single-phase grid-tied inverter system.

TABLE 1. Main Parameters of the Testing System

Symbol	Parameter	Value
v_{dc}	Nominal DC link voltage	400 V
f_{sw}	Switching frequency	20 kHz
L_1	Inverter-side inductance	1.5 mH
C_O	Output capacitance	15 μF
L_2	Grid-side inductance	0.55 mH
S_N	Nominal power	3 kVA
v_N	Nominal voltage	220 V

To fully demonstrate the proposed performance monitor, four groups of experimental tests were performed as follows:

  i) *Stand-alone test*: The monitor is detached from the control system and operates alone for verifying the principle and functions of the proposed monitor itself;

  ii) *Systematic test*: The monitor operates together with the control system for proving the monitor's comprehensive performance (i.e., steady-state, dynamic and harmonics rejection performance);

  iii) *Monitor's interference test*: The control system operates with the proposed monitor enabled and disabled for evaluating the monitor's interference to the power system under test.

  iv) *Comparative test*: The proposed monitor is compared with other loop gain monitoring methods for evaluating the satisfying performance of the proposed monitor.

A. STAND-ALONE TEST

In this test, two predefined sinusoidal signals $x_{in}(t) = 0.5 \sin(1000 * 2\pi * t)$ and $x_{out}(t) = 0.5 \sin(1000 * 2\pi * t + 60°)$ are feed into the proposed control performance monitor. Tested results are shown in Fig. 11(a)–(c).

As verified in Fig. 11(a), a pair of standard quadrature signals $(x_{in-dv}(t), x_{in-qv'}(t))$ with respect to the input signal $x_{in}(t)$ are generated by the signal extractor. Fig. 11(b) shows the respective quadrature waveforms of $x_{in}(t)$ and $x_{out}(t)$, based on which, their frequencies and PMs are calculated

as shown in Fig. 11(c). The estimated frequency and PM are same as the given values, effectiveness of the proposed monitor is therefore proved.

B. SYSTEMATIC TEST

In this test, the proposed monitor works collaboratively with the single-phase inverter system (see Fig. 1). For comprehensive evaluation of the proposed monitor, a series of critical working conditions are designed by adjusting the value of grid impedance. Specifically, a self-designed impedance box, with two serially connected inductor (0.5 mH, 0.1 Ω) modules controlled by respective relays, is connected in series with the grid emulator (Chroma 61830) as shown in Fig. 10. Leveraging on which, the grid impedance is varied among three cases (Case 1: 0.1 Ω + 0 mH; Case 2: 0.2 Ω + 0.5 mH; Case 3: 0.3 Ω + 1 mH) and the grid voltage is superimposed with 5% of the 5th and 5% of the 7th harmonics. The tested results are shown in Fig. 11(d), (e) and (f).

  i) *Steady-state performance:* In order to evaluate the accuracy of the proposed monitor, control indexes monitored from the experiments are compared to those calculated by the theoretical transfer function derived in (3). Two test cases with different grid impedances are discussed herein: Case 1 emulates the ideal grid ($Z_G = 0.1 Ω + 0$ mH) while case 2 represents the weak grid ($Z_G = 0.2 Ω + 0.5$ mH).

  Step responses of Case 1 and Case 2 are compared from experiments, simulations and theoretical calculations, as shown in Fig. 12. It is easy to notice a close match both in terms of the obtained waveforms and the measured rise time and overshoots. Finally, after comparing the theoretical calculated results with the experimental results, only minor errors of less than 0.5% and 5% are observed in BW and PM, respectively.

  ii) *Dynamic performance*: The grid impedance variations are performed by a digitally controlled grid impedance emulation box which is connected in series between the grid emulator and the inverter. As can be seen from Fig. 11(e) and (f), the proposed monitor is able to ride through the transitions and reach to a new steady-state in only few milliseconds. The proved satisfying dynamic performance demonstrates its applicability in weak grids and even ultra-weak grids.

  iii) *Harmonics rejection performance*: Grid background harmonics usually has significant impacts on the estimation accuracy of loop gain monitors. Since the proposed monitor is designed with superior harmonics attenuation performance, as proved in Fig. 11(d)–(f), the monitor can perform normally, estimating the control performance indexes accurately even under severely polluted grid conditions.

C. MONITOR'S INTERFERENCE TEST

To evaluate the influence of the perturbating signal (x_p) on system's power quality, the waveform of the grid current i_G with the proposed monitor enabled and disabled are shown
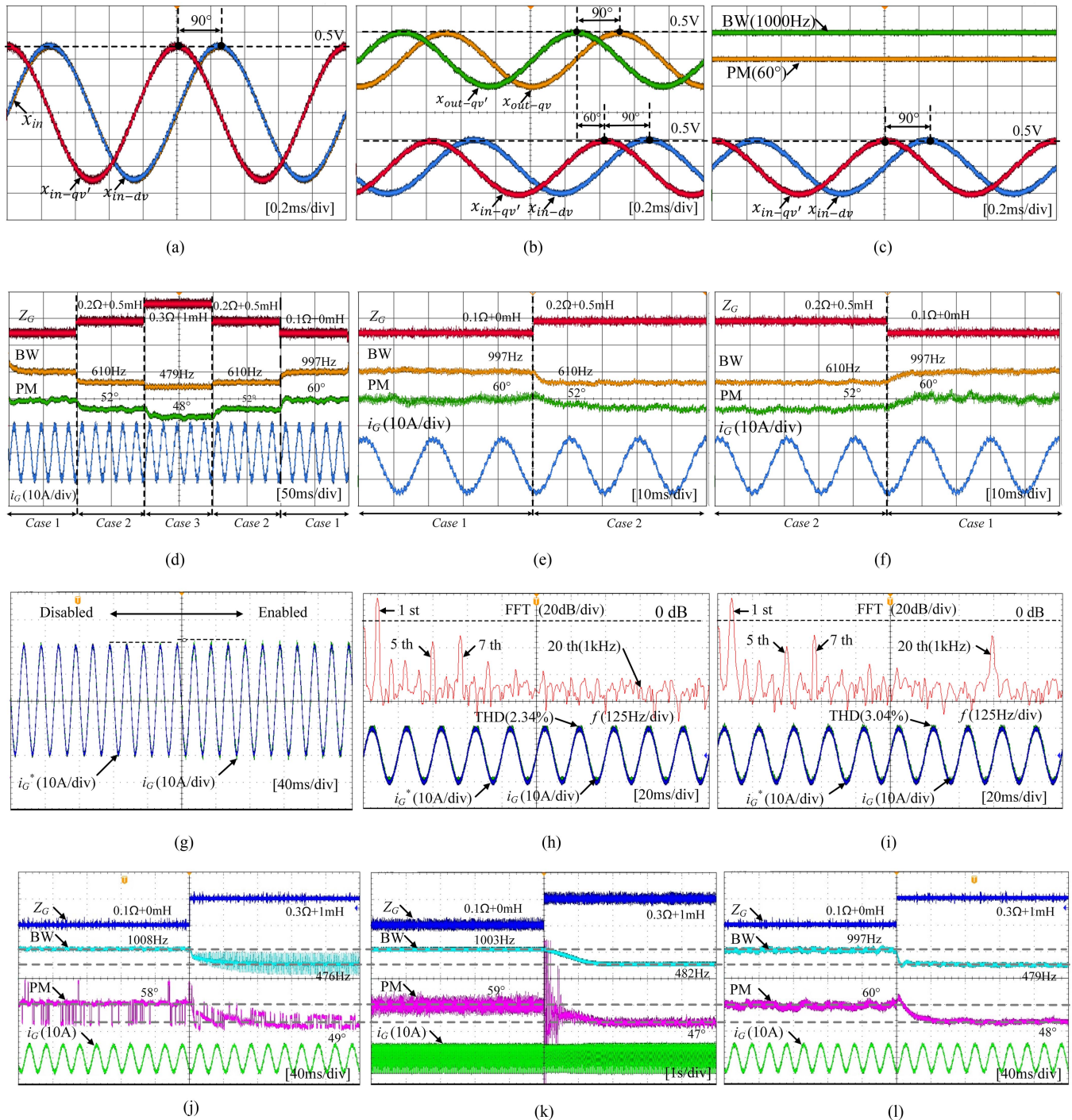
FIGURE 11. Experimental results: (a) Input and output signals of the signal extractor; (b) generated quadrature signals of x_{in} and x_{out}; (c) measured BW and PM of the stand-alone test; (d) measured BW and PM of the closed-loop test under grid impedance variations (case 1: 0.1 Ω + 0 mH; case 2: 0.2 Ω + 0.5 mH; case 3: 0.3 Ω + 1 mH) and grid harmonics (5% of 5th and 5% of 7th); (e) and (f) zoomed-in views of (d); (g) output waveforms with the proposed monitor enabled and disabled; (h) and (i) are the respective zoomed-in views and the corresponding FFT results of (g); measured BW and PM from case 1 to case 3 with different methods: (j) Method from [18]; (k) method from [12] (l) proposed method.

in Fig. 11(g). Fig. 11(h) and (i) are the respective zoomed-in views and the corresponding FFT results. From which, it is evident to notice that when the monitor is enabled, except for the grid harmonics, the perturbating componnet appears in i_G as well. However, the magnitude of the injected signal x_p is small enough which results in only minor distortion, making the grid current THD value slightly increased from 2.34% to 3.04% in this test. Additionally, by performing intermittent monitoring, the interference can be further reduced.
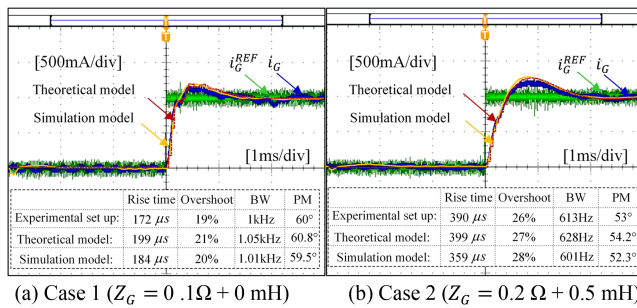
	Rise time	Overshoot	BW	PM
Experimental set up:	172 μs	19%	1kHz	60°
Theoretical model:	199 μs	21%	1.05kHz	60.8°
Simulation model:	184 μs	20%	1.01kHz	59.5°

	Rise time	Overshoot	BW	PM
Experimental set up:	390 μs	26%	613Hz	53°
Theoretical model:	399 μs	27%	628Hz	54.2°
Simulation model:	359 μs	28%	601Hz	52.3°

(a) Case 1 ($Z_G = 0.1\Omega + 0$ mH)   (b) Case 2 ($Z_G = 0.2\Omega + 0.5$ mH)

FIGURE 12. Step responses of the grid current loop obtained from experiments, simulations and theoretical calculations.

D. COMPARATIVE TEST

In order to evaluate the performance of the proposed monitor, the widely used projection-based method [12] and the peak sampling method [18] are used for comparison. Specifically, the grid impedance is varied from Case 1 ($Z_G = 0.1 \Omega + 0$ mH) to Case 3 ($Z_G = 0.3 \Omega + 1$ mH) to emulate the scenario changes between stiff and weak grids. To be fair, amplitudes of the injected signal and calculation periods are designed same. Measured BW, PM as well as grid current results of different methods are shown in Fig. 11(j)–(l).

From the steady-state performance point of view, the projection based monitor (Fig. 11(k)) and the proposed monitor (Fig. 11(l)) are better than the peak sampling method (Fig. 11(j)) with flat and smooth BW and PM results. That's because the zero-crossing detection technology is used in the peak sampling method for phase detection, which is very sensitive to the sampling frequency and background harmonics. By comparison, it is obvious to observe the superior dynamic performance of the proposed method. The transition of the proposed monitor (Fig. 11(l)) is performed within 10 ms, which is about 100 times faster than the projection based method (Fig. 11(k)).

VI. CONCLUSION

A rapid online control performance monitor is proposed in this work for power converters in weak grids. Its purpose is to acquire power converters' BW and PM continuously without breaking the loop in AC microgrids. The monitor's structure, small-signal model and design criteria are detailed introduced in this article. Theories and experiments have confirmed that the proposed monitor can complete the measurement in just milliseconds with high precision (>98%) even under severe grid harmonics. Furthermore, it also serves as a promising solution for monitoring system operation, conducting converter's diagnostics and health check and adapting behavior of power converters to system environmental changes.

REFERENCES

[1] "2006 IEEE power engineering society general meeting," in *Proc. IEEE Power Eng. Soc. Gen. Meeting*, 2006.

[2] C. Charalambous, C. N. Papadimitriou, A. Polycarpou, and V. Efthymiou, "A Technoeconomical evaluation of a hybrid AC/DC microgrid—The University of Cyprus nanogrid," in *Proc. IEEE 2nd Int. Conf. Ind. Electron. Sustain. Energy Syst.*, 2020, pp. 240–246.

[3] M. Shahidehpour, Z. Li, W. Gong, S. Bahramirad, and M. Lopata, "A hybrid AC/DC nanogrid: The keating hall installation at the Illinois Institute of Technology," *IEEE Electrific. Mag.*, vol. 5, no. 2, pp. 36–46, Jun. 2017.

[4] X. Zhang, C. Liu, R. Ma, H. Bai, F. Gechter, and F. Gao, "Instability of grid connected converter under weak AC grid conditions," in *Proc. IEEE Transp. Electrific. Conf. Expo.*, 2019, pp. 1–5.

[5] Q. Liu, T. Caldognetto, and S. Buso, "Review and comparison of grid-tied inverter controllers in microgrids," *IEEE Trans. Power Electron.*, vol. 35, no. 7, pp. 7624–7639, Jul. 2020.

[6] Q. Liu, T. Caldognetto, and S. Buso, "Flexible control of interlinking converters for DC microgrids coupled to smart AC power systems," *IEEE Trans. Ind. Electron.*, vol. 66, no. 5, pp. 3477–3485, May 2019.

[7] M. Liserre, R. Teodorescu, and F. Blaabjerg, "Stability of photo-voltaic and wind turbine grid-connected inverters for a large set of grid impedance values," *IEEE Trans. Power Electron.*, vol. 21, no. 1, pp. 263–272, Jan. 2006.

[8] M. Lu, A. Al-Durra, S. M. Muyeen, S. Leng, P. C. Loh, and F. Blaabjerg, "Benchmarking of stability and robustness against grid impedance variation for LCL-filtered grid-interfacing inverters," *IEEE Trans. Power Electron.*, vol. 33, no. 10, pp. 9033–9046, Oct. 2018.

[9] M. Li et al., "The control strategy for the grid-connected inverter through impedance reshaping in q-axis and its stability analysis under a weak grid," *IEEE J. Emerg. Sel. Topics Power Electron.*, vol. 9, no. 3, pp. 3229–3242, Jun. 2021.

[10] H. Wang, Y. Chen, W. Wu, Z. Wang, G. Li, and Z. Xie, "Resonance suppression method for grid-connected inverter based on feedforward loop and current loop impedance reshaping under weak grid," in *Proc. IEEE 1st Int. Power Electron. Appl. Symp.*, 2021, pp. 1–9.

[11] J. Morroni, R. Zane, and D. Maksimović, "Design and implementation of an adaptive tuning system based on desired phase margin for digitally controlled DC–DC converters," *IEEE Trans. Power Electron.*, vol. 24, no. 2, pp. 559–564, Feb. 2009.

[12] Q. Liu, T. Caldognetto, and S. Buso, "Stability analysis and auto-tuning of interlinking converters connected to weak grids," *IEEE Trans. Power Electron.*, vol. 34, no. 10, pp. 9435–9446, Oct. 2019.

[13] R. D. Middlebrook, "Measurement of loop gain in feedback systems," *Int. J. Electron. Theor. Exp.*, vol. 38, no. 4, pp. 485–512, 1975.

[14] F. Gonzalez-Espin, E. Figueres, G. Garcera, R. Gonzalez-Medina, and M. Pascual, "Measurement of the loop gain frequency response of digitally controlled power converters," *IEEE Trans. Ind. Electron.*, vol. 57, no. 8, pp. 2785–2796, Aug. 2010.

[15] J. Castello and J. M. Espi, "DSP implementation for measuring the loop gain frequency response of digitally controlled power converters," *IEEE Trans. Power Electron.*, vol. 27, no. 9, pp. 4113–4121, Sep. 2012.

[16] T. Roinila, H. Abdollahi, and E. Santi, "Frequency-domain identification based on pseudorandom sequences in analysis and control of DC power distribution systems: A review," *IEEE Trans. Power Electron.*, vol. 36, no. 4, pp. 3744–3756, Apr. 2021.

[17] A. Barkley and E. Santi, "Improved online identification of a DC–DC converter and its control loop gain using cross-correlation methods," *IEEE Trans. Power Electron.*, vol. 24, no. 8, pp. 2021–2031, Aug. 2009.

[18] J. Morroni, R. Zane, and D. Maksimović, "An online stability margin monitor for digitally controlled switched-mode power supplies," *IEEE Trans. Power Electron.*, vol. 24, no. 11, pp. 2639–2648, Nov. 2009.

[19] A. Khodamoradi, G. Liu, P. Mattavelli, T. Caldognetto, and P. Magnone, "Analysis of an online stability monitoring approach for DC micro-grid power converters," *IEEE Trans. Power Electron.*, vol. 34, no. 5, pp. 4794–4806, May 2019.

[20] A. Khodamoradi, G. Liu, and P. Mattavelli, "Online controller tuning for DC microgrid power converters with the ability to track maximum allowable bandwidth," *IEEE Trans. Ind. Electron.*, vol. 69, no. 2, pp. 1888–1897, Feb. 2022.

[21] A. Riccobono et al., "Stability of shipboard DC power distribution: On-line impedance-based systems methods," *IEEE Electrific. Mag.*, vol. 5, no. 3, pp. 55–67, Sep. 2017.

[22] A. Urtasun, J. Samanes, E. L. Barrios, and P. Sanchis, "Control design and stability analysis of power converters: The discrete generalized bode criterion," *IEEE Access*, vol. 9, pp. 37840–37854, 2021.

[23] J. Sun, "Impedance-based stability criterion for grid-connected inverters," *IEEE Trans. Power Electron.*, vol. 26, no. 11, pp. 3075–3078, Nov. 2011.

[24] R. Guzman, L. G. de Vicuña, M. Castilla, J. Miret, and H. Martín, "Variable structure control in natural frame for three-phase grid-connected inverters with LCL filter," *IEEE Trans. Power Electron.*, vol. 33, no. 5, pp. 4512–4522, May 2018.

[25] K. Ramakrishnan and N. Swarnalakshmi, "Impact of gain and phase margins on stability of networked micro-grid frequency control system," in *Proc. IEEE 4th Int. Conf. Elect. Energy Syst.*, 2018, pp. 126–132.

[26] S. Buso, T. Caldognetto, and Q. Liu, "Analysis and experimental characterization of a large-bandwidth triple-loop controller for grid-tied inverters," *IEEE Trans. Power Electron.*, vol. 34, no. 2, pp. 1936–1949, Feb. 2019.

[27] R. D. Middlebrook, "Input filter considerations in design and application of switching regulators," in *Proc. IEEE Ind. Appl. Soc. Annu. Meeting*, Oct. 1976, pp. 366–382.

[28] *IEEE Standard for Interconnection and Interoperability of Distributed Energy Resources with Associated Electric Power Systems Interfaces*, IEEE Standard, 2018.

[29] Z. Xin, P. C. Loh, X. Wang, F. Blaabjerg, and Y. Tang, "Highly accurate derivatives for LCL-filtered grid converter with capacitor voltage active damping," *IEEE Trans. Power Electron.*, vol. 31, no. 5, pp. 3612–3625, May 2016.

[30] R. Teodorescu, M. Liserre, and P. Rodríguez, *Grid Converters for Photovoltaic and Wind Power Systems*. Hoboken, NJ, USA: Wiley, 2011.

JIACHEN WANG (Student Member, IEEE) received the B.S. degree in electrical engineering in 2019 from the Hebei University of Technology, Tianjin, China, where he is currently working toward the Ph.D. degree in electrical engineering.

His research interests include power electronic converter's modeling and health monitoring.

QING LIU (Member, IEEE) received the B.S. and M.S. degrees in electrical engineering from the School of Automation, Northwestern Polytechnical University, Xi'an, China, in 2012 and 2015, respectively, and the Ph.D. degree from the University of Padova, Padova, Italy, in 2019.

Since 2020, she has been a Researcher with the Department of Electrical Engineering, Hebei University of Technology, Tianjin, China. Her main research interests include low-voltage microgrids and digital control of power electronic converters.

XIANGCHEN ZENG received the B.S. degree in electrical engineering from the Qingdao University of Science and Technology, Qingdao, China, in 2021. He is currently working toward the M.S. degree in electrical engineering with the Hebei University of Technology, Tianjin, China.

His research interests include grid-connected inverter's stability analysis and improvement strategy.

WEIJIAN HAN (Member, IEEE) received the B.S., M.S., and Ph.D. degrees in electrical engineering from the School of Automation, Northwestern Polytechnical University, Xi'an, China, in 2012, 2015, and 2019, respectively. From 2016 to 2018, he was a Visiting Ph.D. Student with the Department of Information Engineering, University of Padova, Padova, Italy.

Since 2020, he has been a Researcher with the Department of Electrical Engineering, Hebei University of Technology, Tianjin, China. His research interests include modeling and digital control of power electronic converters.

ZHEN XIN (Member, IEEE) received the B.S. and M.S. degrees from the College of Information and Control Engineering, China University of Petroleum, Qingdao, China, in 2011 and 2014, respectively, and the Ph.D. degree from Aalborg University, Aalborg, Denmark, in 2017.

In 2016, he was a Visiting Scholar with the University of Padova, Padova, Italy. From 2017 to 2018, he was a Postdoctoral Research Fellow with The Chinese University of Hong Kong, Hong Kong. Since 2018, he has been a Professor with the Hebei University of Technology, Tianjin, China. His research interests include condition monitoring of WBG-based power-electronic systems, modeling and validation of power electronic component failure mechanisms, and modeling and control of power converters for renewable energy systems.